Biophysical Journal
Article

Biophysical Society

Domain- and state-specific shape of the electric field tunes voltage sensing in voltage-gated sodium channels

Andrei Y. Kostritskii[1,2,*] and Jan-Philipp Machtens[1,2,*]
[1]Institute of Biological Information Processing (IBI-1), Molekular- und Zellphysiologie, and JARA-HPC, Forschungszentrum Jülich, Jülich, Germany and [2]Institute of Clinical Pharmacology, RWTH Aachen University, Aachen, Germany

ABSTRACT The ability to sense transmembrane voltage underlies most physiological roles of voltage-gated sodium (Nav) channels. Whereas the key role of their voltage-sensing domains (VSDs) in channel activation is well established, the molecular underpinnings of voltage coupling remain incompletely understood. Voltage-dependent energetics of the activation process can be described in terms of the gating charge that is defined by coupling of charged residues to the external electric field. The shape of the electric field within VSDs is therefore crucial for the activation of voltage-gated ion channels. Here, we employed molecular dynamics simulations of cardiac Nav1.5 and bacterial NavAb, together with our recently developed tool *g_elpot*, to gain insights into the voltage-sensing mechanisms of Nav channels via high-resolution quantification of VSD electrostatics. In contrast to earlier low-resolution studies, we found that the electric field within VSDs of Nav channels has a complex isoform- and domain-specific shape, which prominently depends on the activation state of a VSD. Different VSDs vary not only in the length of the region where the electric field is focused but also differ in their overall electrostatics, with possible implications in the diverse ion selectivity of their gating pores. Due to state-dependent field reshaping, not only translocated basic but also relatively immobile acidic residues contribute significantly to the gating charge. In the case of NavAb, we found that the transition between structurally resolved activated and resting states results in a gating charge of $8e$, which is noticeably lower than experimental estimates. Based on the analysis of VSD electrostatics in the two activation states, we propose that the VSD likely adopts a deeper resting state upon hyperpolarization. In conclusion, our results provide an atomic-level description of the gating charge, demonstrate diversity in VSD electrostatics, and reveal the importance of electric-field reshaping for voltage sensing in Nav channels.

SIGNIFICANCE Voltage-gated sodium (Nav) channels play essential roles in electrical signaling in neurons and muscle. Channel gating relies on the coupling between transmembrane voltage and voltage-sensing domains (VSDs), whose activation leads to opening of the central pore. This coupling and thereby the energetics of channel activation are defined by the distribution of the applied voltage across a VSD. Here, we reveal a complex isoform-, domain-, and state-dependent shape of the electric field within VSDs of Nav channels and discuss implications of this variability in various roles of VSDs in Nav functions. Our study emphasizes the impact of electrostatics on functional properties and unveils biophysical details that will lead to a deeper understanding of Nav channels in health and disease.

INTRODUCTION

Voltage-gated sodium (Nav) channels form a key component of electrical signaling in excitable cells by triggering the upstroke phase of the action potential in response to membrane depolarization. Ion conduction of Nav channels, and of other voltage-gated cation channels, is coupled to transmembrane voltage via specialized voltage-sensing domains (VSDs). Each Nav channel contains four VSDs that are either homologous as in eukaryotic channels or identical as in tetrameric bacterial homologs. Membrane depolarization induces conformational changes in VSDs, which in turn convey to the pore module of the channel and trigger its opening. The overall VSD structure is quite conserved across many voltage-dependent proteins such as voltage-gated potassium (Kv) and calcium channels and voltage-sensing phosphatases (VSPs) (1). Generally, a VSD is composed of four helical segments (S1–S4) organized in a

Submitted December 30, 2022, and accepted for publication April 12, 2023.
*Correspondence: a.kostritskii@fz-juelich.de or j.machtens@fz-juelich.de
Editor: Philip Biggin.
https://doi.org/10.1016/j.bpj.2023.04.013

bundle, where S4 plays the main role in voltage sensing. According to the widely accepted "helical-screw" model, activation of Nav channels is caused by vertical translation of S4 across the membrane, which is accompanied by rotation along the helical axis (2). Transmembrane electric field governs the S4 translocation by acting on a stretch of conserved basic residues (mainly arginines) that are regularly distributed along S4. The rotation of the helix is proposed to ensure formation of a proper network of salt bridges between these basic residues and acidic residues on S1–S3 that remain relatively immobile upon VSD activation (3). The inner volume of the VSD has an hourglass shape, where hydrated vestibules of the gating pore are separated by a hydrophobic constriction site (HCS) that is formed by multiple hydrophobic residues and a conserved bulky phenylalanine or tyrosine residue. During activation, the basic residues are translocated across the HCS, leading to an upward helical-screw motion of the VSD (2). Subsequent changes in the pore module of the channel result in its opening and thereby initiate ion conduction through the central pore.

The S4 translocation is associated with a prominent redistribution of charges within a VSD, which leads to a transient gating current that can be measured experimentally (4). By knowing the total number of channels in the system, the integrated gating current can be in turn used to obtain the gating charge Q_g—a charge associated with the activation of a single channel (5). Furthermore, the contribution of an individual residue to the gating charge can be obtained from the change in the gating charge induced by neutralizing substitution of residues (6,7). From an energetics point of view, the gating charge can be considered a measure that links transmembrane voltage to the energy difference between resting and activated states of the channel (8,9). In this case, the gating charge associated with a single residue can be inferred from the state- and voltage-dependent change in the electrostatic potential sensed by the residue (8,9). Thus, the distribution of the electrostatic potential across the VSD in different states directly relates to the gating charge and energetics of channel activation. In accord with that, experimental studies on potassium channels demonstrated that VSD geometry and ionic strength of the solution affect the gating charge by changing the distribution of the electric field (10). A number of experimental methods have been used to measure the electric field within the VSD (11–13). Yet, none of them have been used to estimate contributions of individual residues to the gating charge. Furthermore, additional mutations together with rather bulky reagents to probe the electric field would likely disturb native dynamics and electrostatic properties of the VSD, thus biasing such estimation.

Atomistic molecular dynamics (MD) simulations based on high-resolution structures of voltage-dependent proteins offer an alternative for obtaining insights into electrostatics of native VSDs. Previous studies on voltage coupling in Kv channels (14–17), as well as in Nav channels (18), and in the VSP from *C. intestinalis* Ci-VSP (18) found no notable change in voltage-fraction distribution across VSDs from different channels (18) nor between different activation states of a single VSD (16,18). Specifically, in these studies, the transmembrane voltage appeared to drop linearly across the central part of the VSD. Yet, the predicted extent of the region with the focused electric field was longer than previous experimental estimates of about 4 Å (13,19). Notably, these results were based on low-resolution electrostatics calculations that, as we have shown recently (20), could result in qualitatively poor electrostatic-potential distributions. For reliable and convergent quantification of electrostatics from MD simulations, we have recently developed the *g_elpot* tool (20), which provides high-resolution insights into biomolecular electrostatics (20–23). Hydration of charged residues and vestibules of VSDs justifies usage of *g_elpot*, which requires the presence of water molecules in the analyzed regions, for obtaining information on electric-field distribution in voltage-sensitive regions of VSDs. Here, we additionally extended functionality of the tool so that it could extract the potential within an arbitrary atom group, e.g., at the charged tip of a residue, to directly measure voltage fraction sensed by individual residues. Apart from quantification of voltage coupling, detailed analysis of VSD electrostatics yields insights into ion selectivity of so-called gating pores that can be formed by VSDs either in response to pulsed electric fields (24) or upon introduction of certain VSD mutations implicated in a number of channelopathies (25–29).

In addition to high-resolution quantification of electrostatics, MD simulations can be used to calculate the overall gating charge given that the structures of different states are available. Several approaches for gating-charge calculations have been suggested (30,31), among which a method based on charge-displacement calculations (the so-called Q-route) is the most widely used one (15,16,30,32–34), and the approach utilizing computational electrophysiology (CompEL) (35) simulations most closely resembles experimental conditions (31,36–38). Such analysis is perfectly suitable for directly relating structurally resolved states of a channel with experimental measurements of the gating charge. Thus, recent progress in structural characterization of Nav channels (39–47), and in particular the first resting-state structure of a bacterial NavAb channel from *Arcobacter butzleri* (43), make it now possible to assess details of voltage coupling and gating charge in Nav channels with atomistic resolution.

Here, we used MD simulations of NavAb and Nav1.5 to quantify electrostatics of Nav VSDs, thereby obtaining atomic-level insights into their voltage coupling and gating charge. We found that the shape of the electric field within VSDs varies prominently across different isoforms and domains, with notable reshaping upon transition between the activation states. Moreover, the quantification of electrostatics allowed us to shed some light on ion selectivity of

VSD pores and energetics of the gating-pore conduction. Finally, we used multiple approaches to calculate Q_g between the resolved activated and resting states of NavAb to demonstrate that knowing the electrostatic-potential profile along the hydrated regions of a VSD is sufficient to estimate its gating charge. We found that the resulting Q_g of about 8e is significantly lower than experimental values, suggesting that at least one of the resolved structures represents only an intermediate activation state. Based on the analysis of electrostatic-potential distribution within the VSD, we propose that a hyperpolarization-induced deeper resting state would be electrostatically more favorable than a depolarization-induced higher activated state.

MATERIALS AND METHODS

Protein models

The activated and resting states of NavAb were modeled based on a crystal structure with PDB: 6P6X and a cryo-electron microscopy (cryo-EM) structure with PDB: 6P6W, respectively (43). The cysteine mutations in these structures (G94C and Q150C) were retained as well as the disulfide bond between these residues in the resting-state structure. For the sake of consistency between the protein models, we reverted the KAV mutations (N49K, L109A, and M116V), which were used to shift the voltage dependence of NavAb to determine its resting-state structure (43). The final NavAb model covered residues 1 to 230. Cardiac Nav1.5 was modeled based on the cryo-EM structure with PDB: 6UZ0 (44), where only protein atoms were retained. The disulfide bonds were imposed between the cysteine pairs C281–C336, C327–C342, C909–C918, C1365–C1386, and C1730–C1744. Residues N319, N329, N1382, and N1390 were glycosylated according to the cryo-EM structure (44). The long intracellular loops unresolved in the original structure were omitted so that the final Nav1.5 model contained three polypeptide chains corresponding to domains 1, domain 2, and domains 3 and 4 together, covering residues 121–424, 699–945, and 1190–1780, respectively. The reverse mutations as well as completion of all the models with the atoms missing in the structures were obtained using Modeller v.9.18 (48). In all protein models, the N and C termini were capped with acetyl and N-methylamine, respectively. The standard protonation state at neutral pH was assigned to all residues in all models, except for D1282 in Nav1.5, which points to the membrane interior and was, therefore, modeled in the neutral form.

The following naming convention is used for the gating residues: in NavAb, gating arginines 99, 102, 105, and 108 correspond to R1–R4, respectively. In Nav1.5, VSDs have various numbers of gating residues so that VSD3 and VSD4 have an additional gating residue that precedes those four that are conserved in NavAb. For consistency, the gating residues in VSD3 and VSD4 of Nav1.5 were numbered starting from 0 so that in the resolved activated-state structures of both bacterial and mammalian channels, R3 is located just above the HCS. In VSD1, residues R220, R223, R226, and K229 correspond to R1, R2, R3, and K4. In VSD2, residues R809, R812, R815, K818, and K821 correspond to R1, R2, R3, K4, and K5. In VSD3, residues K1302, R1305, R1308, R1311, R1314, and R1318 correspond to K0, R1, R2, R3, R4, and R5. In VSD4, residues R1625, R1628, R1631, R1634, R1637, and 1640 correspond to R0, R1, R2, R3, R4, and R5.

Simulation details

The simulations were performed using GROMACS 2021 (49) with a time step of 2 fs. A pressure of 1 bar was applied semiisotropically with a time constant of 5 ps using the Parrinello-Rhaman barostat (50) in zero-voltage simulations and the Berendsen barostat (51) in all the other simulations. A temperature of 310 K was maintained with the v-rescale thermostat (52) using a time constant of 0.5 ps. van der Waals interactions were calculated with the Lennard-Jones potential and a cutoff radius of 1.2 nm, with forces smoothly switched to zero in the range of 1–1.2 nm without a dispersion correction. Electrostatic interactions were calculated by the smooth particle mesh Ewald (SPME) method (53,54), with a real-space cutoff distance of 1.2 nm. The protein and lipids were described by the CHARMM36m (55) and CHARMM36 (56) force fields, respectively. All hydrogen-involving bonds were constrained with LINCS (57). Ions were described using CHARMM parameters with the NBFIX correction (58), and the CHARMM TIP3P model was used for water molecules. The protein was embedded in a 1-palmitoyl-2-oleoyl-phosphatidylcholine bilayer using the *g_membed* function (59) in GROMACS. Na^+ and Cl^- were added to the solution with a bulk concentration of approximately 150 mM NaCl. An example of a NavAb simulation system is shown in Fig. 1 *A*.

Each system was equilibrated for 102 ns in four steps: 2 ns with position restraints on all heavy atoms of the protein (in all dimensions) and of the lipids (in the z dimension), 80 ns with only protein heavy atoms restrained, 10 ns with the restrains on the backbone atoms only, and 10 ns with all restraints released. In production runs, each system was simulated for 500 ns. Constant electric-field and CompEL (35) simulations were started from the configuration of the system after 100 ns of the zero-voltage simulations. In the constant electric-field simulations, a field of ± 10 mV/nm along the z dimension was applied, resulting in the overall transmembrane voltage of

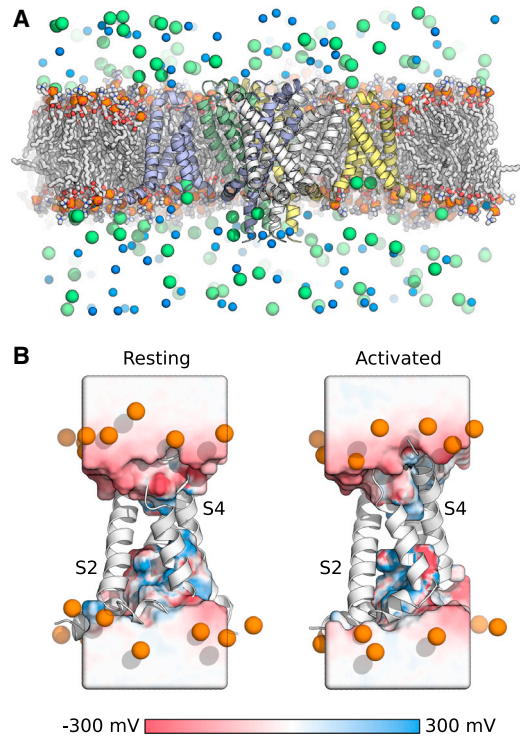

FIGURE 1 NavAb system and distribution of electrostatic potential through its VSD. (*A*) Simulated system of NavAb. Four domains are colored differently. Lipids are shown as sticks, and their phosphorus atoms as orange spheres. Cl^- and Na^+ ions are shown as green and blue spheres, respectively. (*B*) An illustrative example of electrostatic potential distribution within a VSD of NavAb. Shown are water-occupancy maps contoured at 0.1 and colored according to the electrostatic potential as obtained with *g_elpot*. The VSD in the resting and activated states is shown as white cartoon (helices S2 and S4 are labeled). Orange spheres represent phosphorus atoms of lipid headgroups around the VSD. To see this figure in color, go online.

around ±110 and ±140 mV in the NavAb and Nav1.5 systems, respectively. This field was mild enough not to induce any considerable charge translocation across the HCS in any of VSDs, ensuring that the original activation state was preserved. In double bilayer systems used for the Q_g calculations via the CompEL simulations (31), two copies of the system are stacked, with one of them mirrored about the *xy* plane. The charge imbalance between the compartments was created by an unequal number of Cl^- ions in them.

Quantification of electrostatics

Electrostatics and voltage coupling was quantified with *g_elpot* (20); source code, installation instructions, and usage recommendations can be found at https://jugit.fz-juelich.de/computational-neurophysiology/g_elpot. Briefly, *g_elpot* relies on the SPME method and employs explicit water molecules to extract convergent distribution of electrostatic potential of high resolution from atomistic MD simulations. First, the raw potential is calculated on a dense grid by the SPME method using a sufficiently high inverse Gaussian width β of typically 20 nm^{-1}. In this study, the SPME potential was calculated on grids of 304 × 304 × 216 and 312 × 312 × 264 points in NavAb and Nav1.5 systems, respectively. Second, each water molecule is assigned with the potential averaged over a sphere around the water-molecule center of geometry. It is a combination of the high β value together with the exclusion volume of a water molecule that allows for convergent calculation of the electrostatic potential, while taking only its long-range part into account. Finally, the trajectory frame is fitted onto the reference one, and water-molecule potentials are interpolated onto the nodes of the final electrostatic-potential map, which is built around a protein region of interest. The procedure described above is repeated for each frame to extract the average potential distribution. In the present study, we built a map of 0.5 Å resolution around the VSD and used the Cα atoms of S1–S4 as the fitting group. In addition to the electrostatic-potential map, *g_elpot* generates a water-occupancy map that reports on the fraction of frames with a node occupied by water. The electrostatic-potential and water-occupancy maps can be easily combined with, for example, the *gridData* module of the MDAnalysis library (60) to convert potential distribution into one-dimensional profiles, as described previously (20). Briefly, the water-occupancy map was first normalized by the bulk occupancy defined as an average over the most extracellular slab, and the electrostatic-potential map was then masked by the normalized water-occupancy map with a threshold of 0.1. The masked electrostatic-potential map was converted into a one-dimensional profile by averaging the potential in each slab. The potential profile obtained by *g_elpot* reports only on the reaction part of the potential created by the charge distribution in the system. Therefore, in the case of the electric-field application, the profiles were corrected by the potential created by the field with respect to the outermost edge of the electrostatic-potential map in the *z* dimension. In turn, the voltage-fraction profiles were calculated by subtracting the electrostatic-potential profiles upon electric-field application from those at zero voltage and dividing the result by the value of transmembrane voltage.

Originally, *g_elpot* quantified electrostatics only in the hydrated regions of the system. To measure voltage coupling directly for individual residues, we implemented a new functionality to the tool so that the time course of the potential at the center of any atom group could be computed. In particular, the following atom groups (CHARMM naming convention) were used to calculate the potential at ARG (NE, CZ, NH1, NH2), LYS (NZ, HZ1, HZ2, HZ3), GLU (CD, OE1, OE2), ASP (CG, OD1, OD2), TYR (CG, CD1, CD2, CE1, CE2, CZ), and PHE (CG, CD1, CD2, CE1, CE2, CZ). Since only the relative change of the residue potential is relevant for calculating voltage coupling, omission of the residue-specific short-range part of the potential is fully justified. Moreover, for the sake of convenience, the residue potential was subtracted with its value in a bulk solution, which was obtained from a simulation of an isolated amino acid in 150 mM NaCl solution. These bulk values of the potential were −306.6, 3,738.4, −2,052.2, −1,955.7, −880.4, and −1,452.0 mV for Arg, Lys, Glu, Asp, Tyr, and Phe, respectively. Similar to water-molecule potential, that of the residues required correction when an external electric field was applied. However, in the case of the residue potentials, the choice of the reference point for this correction was more arbitrary (see results for details). In practice, it was chosen such that the voltage fractions sensed by the outermost and the innermost charged residues of the VSD were simultaneously as close as possible to zero and one, respectively.

Gating-charge calculations

Here, we used four different approaches to calculate the gating charge associated with the transition of NavAb between its resolved resting and activated states. The first two are based on computing voltage fraction f_i, also known as electrical distance (8,10), sensed by each charged residue *i* in the VSD as

$$f_i \approx \frac{\partial \Phi_i}{\partial V}, \tag{1}$$

where Φ_i is the potential on residue *i* and *V* is the transmembrane voltage. The contribution δq_i of each charged residue into the gating charge is then defined as

$$\delta q_i = q_i\left(f_i^r - f_i^a\right) = q_i \Delta f_i, \tag{2}$$

where q_i is the charge of residue *i* and Δf_i is the difference in voltage fraction sensed by this residue in the resting (f_i^r) and activated (f_i^a) states. The sum of contributions of individual residues gives the overall gating charge

$$Q_g^r = \sum_i \delta q_i^r, \tag{3}$$

where the sum goes over charged residues within the VSD and the superscript *r* indicates calculation of the voltage fraction directly sensed by the residue.

In addition to the directly measured voltage fraction for a residue, we estimated the gating charge using the voltage fraction sensed by water molecules, whose position along the *z* dimension corresponded to that of a residue tip:

$$Q_g^w = \sum_i q_i \Delta f^w(z_i), \tag{4}$$

where Δf^w was defined as the difference in voltage fraction sensed by water molecules, whose positions along the *z* dimension correspond to that of the residue, in the resting and activated states. In practice, the voltage fraction was obtained by interpolating the voltage-fraction profile of water at the average *z* position (z_i) of the tip of the residue *i*.

In the third method, we evaluated the gating charge via the Q-route (15,30), which is based on calculating the displacement charge Q_d as

$$Q_d = \sum_i \frac{q_i z_i^u}{L_z}, \tag{5}$$

where the sum goes over all the atoms in the system, q_i is the charge of atom *i*, L_z is the length of the simulation box in the *z* dimension, and z_i^u is the *z* coordinate of the atom *i* in an unwrapped trajectory. The latter means that no correction for periodic boundary conditions is applied so that upon crossing a box boundary, atoms are not brought back into the box. Based on the displacement charge, the gating charge can be obtained as (15,30)

$$Q_g^d = \langle Q_d \rangle_{a,V} - \langle Q_d \rangle_{r,V}, \tag{6}$$

where averaging $\langle \ldots \rangle_{r,V}$ and $\langle \ldots \rangle_{a,V}$ is done for systems at voltage *V* with the channel in the resting (*a*) or activated (*r*) state, respectively. In practice, the dependence of Q_d on *V* was fit by linear function, and the difference in the intercept values provided an estimate of Q_g^d.

Finally, we used the CompEL method (35) to estimate the gating charge from a double-membrane system (31). Briefly, the dependence of the transmembrane voltage V on an ionic charge imbalance q_{exc} between compartments separated by the membranes is fitted by

$$V = \frac{q_{exc} + 2q_p}{2C_m}, \quad (7)$$

where q_p is the contribution of the protein into the charge imbalance and C_m is the membrane capacitance. In practice, both represent fitting parameters in linear fit of the dependence of transmembrane voltage on the charge imbalance q_{exc}. The q_p value is then extracted from the fitting separately for the channel in the resting (q_p^r) and activated (q_p^a) states, and the gating charge is calculated as

$$Q_g^c = q_p^r - q_p^a. \quad (8)$$

Transferable displacement-charge calculations

Calculation of the displacement charge according to Eq. 5 requires trajectory unwrapping to properly account for periodic boundary conditions (15,30). However, the resulting charge displacement would depend on the initial configuration of the system, which is to be used for the trajectory unwrapping. In particular, positions of mobile ions could have a drastic impact on the charge displacement. For example, if two starting configurations differ in the position of a single ion, being located just below the upper edge of the simulation box in one configuration and just above the lower edge in another, the initial values of the displacement charge in these systems will differ by about $1e$. Notably, since ions remain in one half of the space separated by the bilayer due to the unwrapping, this difference will retain along the whole trajectory, resulting in a seemingly non-zero gating charge for the transition between identical states of the channel. Thus, the direct application of the method requires that the systems differ only in conformation of the protein but not in positioning or the number of nonprotein atoms. In our case, however, not only were the systems with the channel in different states prepared independently, but also our simulations with applied electric field were initiated from the 100 ns frame of the zero-voltage simulations, implying a difference in instantaneous atomic configurations and precluding us from the direct usage of the method.

To make the displacement charge transferable across different systems, we propose a particular treatment of a starting configuration and simulations trajectories used for the displacement-charge calculation. We start with translating all the atoms in the system along the z dimension so that the center of the lipid bilayer is located at zero. Then, we apply periodic boundary conditions to the translated system while keeping all molecules whole. As a result, the system has the extracellular leaflet of the bilayer together with the protein at the bottom of the box, whereas the intracellular leaflet is placed at the top. Provided that a channel does not conduct ions, all of them remain inside the simulation box enclosed by two leaflets of the bilayer, relieving the problem of initial ion positioning. The final unwrapping of the trajectory is, thus, needed only for proper accounting for neutral water molecules crossing the borders of the box. After such pretreatment, the displacement charge calculated by Eq. 5 can be compared between systems started from unequal atomic configurations. Instructions for trajectory preparation as a sequence of *gmx* commands using the GROMACS simulation package (49) can be found in the supporting material.

General analysis details

All quantities were averaged over the last 400 ns of a simulation trajectory. Trajectories were sampled every 100 ps in all the analyses except for the displacement-charge calculations, in which the sampling interval of 20 ps was used, to ensure proper trajectory unwrapping. Data for NavAb were averaged over four protomers from one simulation, and data for Nav1.5 were averaged over three independent simulation replicas. All the profiles along the VSD axis were centered at the Cα atom of the aromatic residue forming the HCS. GROMACS tools, *g_elpot* (20), and in-house python scripts using the MDAnalysis library (60) were used for all analyses. All visualizations were done using PyMOL v.1.8.

RESULTS

Electrostatic potential within VSD of NavAb

We started with quantification of electrostatic potential inside the VSD of NavAb. Fig. 1 *B* illustrates distribution of the electrostatic potential within the hydrated interior of the VSD in resting and activated states, as calculated from the simulations in the absence of voltage. To quantify the difference in electrostatic-potential distributions, we converted the maps into one-dimensional profiles along the z dimension of the system, as shown in Fig. 2, *A* and *B*. Since reliable quantification of electrostatics requires persistent hydration (20), the potential in the poorly hydrated central part of the VSD was associated with high error and therefore was omitted in the profiles. In the resting state, the potential is quite shallow in the intracellular half of the VSD, indicating efficient balancing of positively charged arginines by acidic residues (Fig. 2 *A*). At the same time, only one extracellular arginine (R1) cannot effectively compensate the negative charge of the extracellular acidic residues, so the potential is notably negative in the extracellular vestibule of the VSD in the resting state (Fig. 2 *A*). Upon transition to the activated state, R2 and R3 reduce the depth of the potential well in the extracellular part of the VSD while deepening it in the intracellular part (Fig. 2 *B*). Note that the accumulation of gating arginines in the extracellular vestibule also results in a prominent surge in the potential close to the HCS. Thus, the overall electrostatic potential is less balanced in the activated compared with the resting state of the VSD, in accordance with the energetic cost needed for the channel activation. Finally, concerning the ion selectivity of the VSD, the prominent gradients in the potential in the activated state would create energetic barriers for both anions and cations, whereas the nonpositive potential along the whole VSD in the resting state would imply a stronger cation-selective gating-pore current.

We then analyzed distribution of the electrostatic potential along the VSD upon transmembrane voltage application. Following the electrophysiological convention, we assumed the system to be grounded in the extracellular half, so we set the potential to zero in the most extracellular point of the electrostatic-potential map. The transmembrane potential was induced by applying a constant electric field E_z of ± 10 mV/nm along the z dimension to all atoms in the system (30), resulting in about ± 110 mV transmembrane voltage (Fig. 2, *A* and *B*). Note that the potential computed by *g_elpot* is defined by atom distribution and therefore represents a reaction potential (61) created by the system in response to the external electric field. To

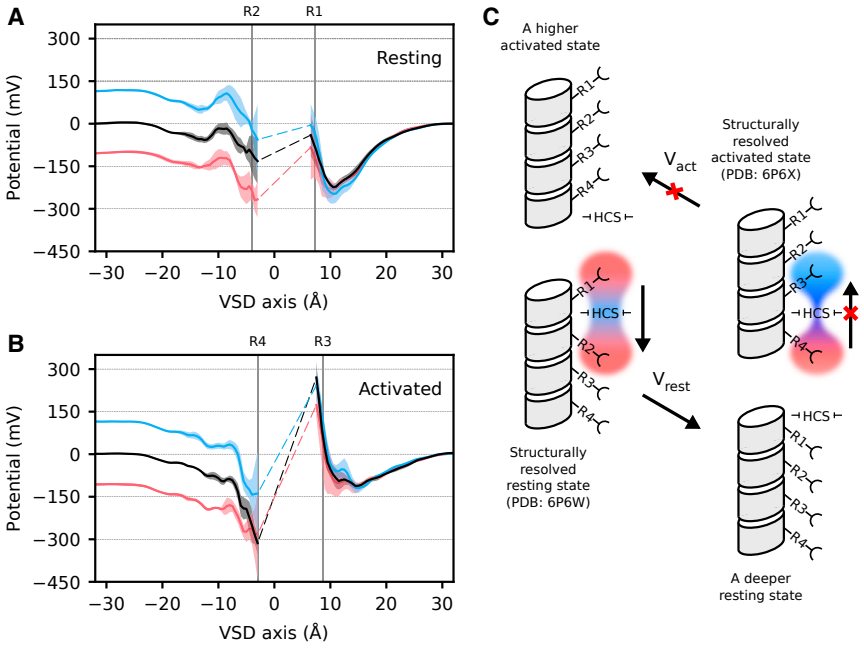

FIGURE 2 State dependency of the electrostatic potential within the VSD of NavAb. (*A* and *B*) Profiles of electrostatic potential in the hydrated regions of the NavAb VSD in the resting (*A*) and activated (*B*) states at 0 (*black*), −110 (*red*), and +110 mV (*blue*) transmembrane voltages. Average positions of the gating arginines that flank the HCS are indicated by vertical lines. Shaded areas indicate the standard error of mean, as calculated for four NavAb domains. Dashed lines are drawn for visual guidance through the low-hydrated (hydrated in < 2 domains) region, which is characterized by high (> 120 mV) standard error of mean potential. The VSD axis is centered at the HCS. (*C*) A schematic illustrating electrostatic-energy costs for further translocation of S4 from the resolved resting and activated states. The regions above and below the HCS are colored according to their electrostatic potential (*red*, negative; *blue*, positive). The width of the transition region indicates height of the electrostatic-energy barrier. Electrostatics both thermodynamically and kinetically favors a deeper resting state over a higher activated state. To see this figure in color, go online.

correct the potential profiles for the electric-field application, we added a linear term between endpoints of the profile with the slope of E_z. As can be seen in Fig. 2, *A* and *B*, the potential profiles keep their overall form upon voltage application, with a rather stable shift in the potential in the intracellular half of the VSD. Note that in the activated state—in contrast to the resting state—the potential remains negative in the region below the HCS even at +110 mV so that it roughly equals that of the extracellular vestibule (Fig. 2 *B*). The region below the HCS corresponds to a so-called gating charge transfer center (GCTC), which is formed by a pair of acidic residues that catalyze translocation of the gating arginines (62). In the resting state, the GCTC is occupied by R2, which is electrostatically destabilized when positive voltage is applied (Fig. 2 *A*). At the same time, a notably negative potential well in the extracellular vestibule of the VSD favors VSD activation by stimulating upward translocation of R1, which is located just above the HCS (Fig. 2 *A*). Application of the negative transmembrane voltage, in turn, reduces the potential in the GCTC, making it electrostatically similar to the extracellular vestibule (Fig. 2 *A*). As a result, a downward translocation of R1 becomes thermodynamically plausible. In the activated state, the potential is negative in the GCTC regardless of the applied voltage (Fig. 2 *B*). Thus, R4 is electrostatically stabilized in the GCTC even at positive voltages, hindering a further upward motion of S4. At the negative voltage, the potential is substantially lower in the GCTC than in the extracellular vestibule, favoring downward translocation of R3 and therefore deactivation of the VSD.

Previous studies (34,63) as well as our analyses of the gating charge, which are discussed in the following sections, indicate the existence of more extreme activation states of the VSDs in NavAb than those resolved experimentally (43). Considering this possibility, we thus propose that a further upward translocation of S4 from the activated state upon depolarization (i.e., at voltages higher than the voltage of half activation of − 98 mV (64,65)) would be electrostatically unfavorable compared with a downward translocation from the resting state upon hyperpolarization. Moreover, a high barrier of positive electrostatic potential across the HCS would prevent transition of the VSD to a higher activated state. We thus conclude, from the electrostatics perspective, a deeper resting state at a hyperpolarizing transmembrane voltage would be both thermodynamically and kinetically more favorable than a higher activated state of NavAb at the depolarizing voltage as illustrated in Fig. 2 *C*. Moreover, a deeper resting state would be in perfect agreement with a recently resolved resting-state structure of VSD1 in Nav1.7 (46).

Voltage coupling in the VSD of NavAb

We then used our electrostatic-potential profiles to calculate voltage coupling within the VSD of NavAb. For each profile at applied electric field, we subtracted a zero-voltage profile and divided the result by the transmembrane voltage. As a result, we obtained the distribution of the voltage fraction sensed by water molecules within the VSD, as shown in Fig. 3 (*black profiles*). Similar to that of the electrostatic potential, the distribution of the voltage coupling demonstrates dependence on the activation state of the VSD. In particular, the voltage fraction sensed by the VSD starts to increase at about 10 Å above the HCS in the resting state and at about

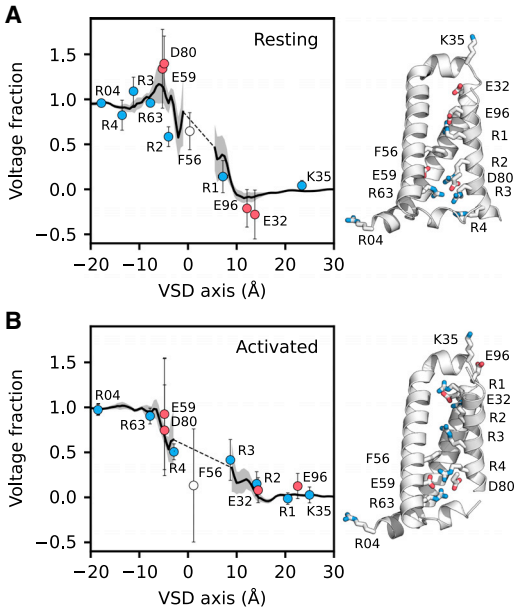

FIGURE 3 Voltage coupling within the VSD of NavAb. (*A* and *B*) Fraction of transmembrane voltage sensed by water and selected residues within the VSD in the resting (*A*) and activated (*B*) states are shown together with the structure of the VSD in the corresponding state. The S3 helix is omitted for clarity. Profiles of the voltage fraction sensed by water molecules within the VSD are shown in black. Data points report on the voltage fraction sensed by labeled charged residues of the VSD. Data for positively and negatively charged residues are shown in blue and red, respectively. Whiskers and shaded areas indicate the standard error of mean as calculated for four NavAb domains. Dashed lines are drawn for visual guidance through the low-hydrated (hydrated in <2 domains) region, which is characterized by high (>0.3) standard error of mean voltage fraction. The VSD axis is centered at the HCS. To see this figure in color, go online.

15 Å in the activated state when approaching the HCS from the extracellular side (Fig. 3, *A* and *B*). Therefore, the increase in the voltage fraction is steeper in the resting compared with the activated state. Moreover, in contrast to the activated state, the voltage fraction in the resting state was characterized by a local bump in the intracellular part of the VSD. The average voltage fraction in that region was higher than one, indicating an excessive focusing of the electric field (Fig. 3 *A*). In other words, upon voltage application, the change in the potential sensed by water molecules in that region exceeded the overall transmembrane voltage.

The results discussed so far are based on the electrostatic potential calculated within water molecules that populate the interior of the VSD. To test if voltage coupling of water molecules is representative of that of VSD residues, we then calculated voltage fraction sensed by individual residues. To this end, we extended original functionality of *g_elpot*, which had been limited to water-molecule potentials, to measure the time course of the potential within any group of atoms, e.g., heads of side chains (see materials and methods for details). Note that according to Eq. 1, only relative change in the electrostatic potential is needed to calculate voltage fraction, justifying usage of only the long-range part of the potential, as done in *g_elpot* (20). Once the potential on a residue has been calculated at different transmembrane voltages, its voltage dependence can be linearly fitted, with the slope of this fit representing the voltage fraction sensed by the residue (Fig. S1). Similar to water potential, that of the residues has to be corrected for the direct contribution from the applied electric field. However, whereas any point in the bulk solution can be used as a reference for the water-potential correction, the choice of the reference point for the residue potential can be arbitrary. The correction potential (Φ_{corr}) is defined by the distance from the reference point (Δz) as $\Phi_i^{corr} = E_z \Delta z_i$, and, taking into account that $V = E_z L_z$, the contribution of the correction potential to the voltage fraction is

$$f_i^{corr} = \frac{\partial \Phi_i^{corr}}{\partial V} = \frac{\Delta z_i}{L_z}. \quad (9)$$

Thus, the position of the reference point along the z dimension directly affects the slope of the potential-voltage dependence and therefore the resulting voltage fraction. To set the reference point for the residue potentials, we first identified R04 and K35 as charged residues with the most intracellular and the most extracellular locations in the VSD, respectively. These residues were assumed to sense either full (R04) or no (K35) transmembrane voltage. We then iteratively changed the position of the reference point along the z dimension and calculated the voltage fraction of these two residues. The iterations were considered finished once the voltage fraction, averaged over four domains, was as close as possible to one for R04 and to zero for K35 at the same time. The obtained reference points (5.7 and 5.3 nm above the HCS in the resting and activated systems, respectively) were used to correct the potential of other VSD residues, resulting in the potential-voltage dependence shown in Fig. S1 for charged residues located in the transmembrane region of the VSD as well as for F56 that forms the HCS.

The resulting voltage fraction sensed by charged residues pointing to the VSD interior is shown in Fig. 3 for the resting and activated states. Notably, the gating arginine located in the GCTC just below the HCS (R2 in the resting state and R4 in the activated state) senses only half of the transmembrane voltage, indicating an incomplete voltage drop across the HCS. Furthermore, in the activated state, R3 and R4 demonstrate similar levels of voltage coupling, suggesting that the S4 downward translocation upon membrane polarization would be governed by both these residues. Importantly, the voltage fraction calculated for individual residues follows all the trends in the profile calculated based on the water potential (Fig. 3). In particular, in the resting state, residues E59 and D80, which form a so-called intracellular negatively charged (INC) center (3), sense a voltage that is higher than the transmembrane one. Despite

pronounced interdomain variation of the voltage fraction in the INC, D80 experienced a voltage fraction higher than one in three out of four NavAb domains. In line with the higher error of mean voltage fraction, the same effect was observed in only two domains in case of E59. Yet, the average voltage sensed either by water molecules in the INC or by its residues demonstrates a clear trend in exceeding the transmembrane voltage. In accord, high voltage sensitivity of the INC residues has been previously detected in a global voltage-sensitivity analysis (66). Upon closer inspection of this region, we found that voltage application slightly changes the arrangement of a salt-bridge network between residues E59, D80, R2, and R63 (Fig. S2 *A*). More specifically, analysis of the distance between these residues demonstrated that an increase in voltage stabilized the bridge between D80 and R2 while destabilizing that between D80 and R63 (Fig. S2 *B*). In agreement with the data on voltage fraction, a less pronounced voltage dependence was observed in the case of the bridge formed by E59 with R2 but not with R63 (Fig. S2 *B*). No clear signs of voltage-induced salt-bridge stabilization/destabilization were observed in the activated-state simulations (Fig. S2 *C*). We therefore propose that the salt-bridge rearrangement could strengthen the electric field sensed by the INC in the resting state. To test this, we conducted an additional simulation of NavAb in the resting state, where the protein structure was restrained. Analysis of this simulation demonstrated that although the main features of the electrostatic-potential profile across the VSD remain similar to the unrestrained simulations (Fig. S3 *A*), the voltage-fraction distribution alters significantly (Fig. S3 *B*). In particular, in the restrained system, the voltage fraction sensed by the INC was < 1, underscoring the significance of the voltage-dependent side-chain rearrangement for the excessive focusing of the electric field.

Gating charge of NavAb

Once the voltage coupling of charged residues within VSD was evaluated in both activation states, we could calculate its gating charge via Eq. 3. For each charged residue, we calculated its contribution to the gating charge using the voltage fraction either sensed by the residue directly or interpolated from the profiles of water-molecule potential (see materials and methods for details). Table 1 shows the gating-charge contributions calculated either via the first (δq^r) or via the second (δq^w) approach. Despite a certain level of deviation between the two approaches, the main features of the gating charge distribution remain the same. In particular, R2 and R3 account for the largest portion of the gating charge among all the gating arginines, similar to the Shaker K^+ channel (15,67). The total gating charge associated with translocation of R2 and R3 is, however, lower than $2e$, indicating that these residues cross only part of the transmembrane voltage upon transition between the resting and activated states. Contribution of the other two gating arginines, R1 and R4, is less pronounced and constitutes less than $1e$. Interestingly, E32 and E96, which are located at the extracellular part of the VSD, have moderate positive contributions to the gating charge, whereas E59 and D80, which point to the intracellular vestibule, exhibit negative gating charges (Table 1). The negative gating charge of E59 and D80 compensates about 0.8-$1e$ of the gating charge associated with S4 translocation. Note that these residues are located on the relatively immobile S2 and S3 helices, respectively, so that they do not cross the electric field upon the activation (Fig. 3). Thus, their prominent contribution to the gating charge results mainly from the electric-field reshaping in the intracellular vestibule of the VSD.

TABLE 1 Contribution of charged residues within the VSD of NavAb to the gating charge

Residue	δq^r (e)	δq^w (e)
R1	0.16 ± 0.20	0.44 ± 0.38
R2	0.43 ± 0.19	1.13 ± 0.17
R3	0.68 ± 0.13	0.62 ± 0.33
R4	0.32 ± 0.24	0.27 ± 0.30
R63	0.06 ± 0.09	0.11 ± 0.13
E32	0.36 ± 0.26	0.10 ± 0.09
E59	-0.41 ± 0.36	-0.46 ± 0.28
E96	0.34 ± 0.21	0.08 ± 0.03
D80	-0.65 ± 0.29	-0.37 ± 0.20

The contribution of each residue was calculated using voltage fraction either directly sensed by a residue (δq^r) or by nearby water molecules (δq^w).

Gating charges of the whole channel calculated from the voltage fraction sensed by residues (Q_g^r) or by water molecules (Q_g^w) are shown in Table 2. Although these two methods provide the average values of Q_g that differ by more than $2e$, this difference lies within the range of rather high errors of mean, which result from strong (hundreds of millivolts) fluctuations in the underlying electrostatic potential (20). Due to the steep dependence of the electrostatic potential on distance, these fluctuations are mainly caused by atoms closest to the point where the potential is calculated. In the high-resolution quantification of electrostatics with *g_elpot*, the contribution of these atoms is properly taken into account so that even small atomic rearrangements lead to prominent change in the potential as we

TABLE 2 Gating charge associated with the transition of NavAb between the structurally resolved resting and activated states

Q_g^r (e)	Q_g^w (e)	Q_g^d (e)	Q_g^c (e)
5.07 ± 2.60	7.67 ± 3.19	8.21 ± 0.17	7.94 ± 0.14

The gating charge was estimated either through the voltage fraction directly sensed by VSD residues according to Eq. 3 (Q_g^r), through the voltage fraction sensed by water molecules according to Eq. 4 (Q_g^w), through the displacement-charge calculations according to Eq. 6 (Q_g^d), or through the CompEL method according to Eq. 8 (Q_g^c).

demonstrated in the previous section (Fig. S3). To obtain a more confined estimate of the gating charge, we then used two system-level approaches, which, however, provide no detailed information on the gating-charge distribution.

First, we followed the Q-route (30) and calculated the displacement charge (Q_d) in our systems. Briefly, the gating charge Q_g^d is defined according to Eq. 6 as the difference in Q_d between systems containing the channel in the resting and activated states. Importantly, this approach requires unwrapping of a simulation trajectory before the calculations to properly account for periodic boundary conditions (15,30). However, the unwrapping itself and the resulting displacement charge depend on the initial configuration of mobile ions in the system. To make the displacement charge transferable across different systems, we propose a particular treatment of a starting configuration and simulations trajectories used for the displacement-charge calculation (see materials and methods for details). Briefly, we virtually confine mobile ions within the unit cell by translating the system along the z dimension so that membrane leaflets are located at the opposite edges of the cell (Fig. 4 *A*). As a result, the displacement charge Q_d calculated from the unwrapped trajectory can be compared between systems with unequal starting positions of ions. Fig. 4 *B* shows time courses of Q_d in the systems with NavAb in the resting and activated states at different voltages. Clearly, voltage application leads to redistribution of mobile charges in the system and altered displacement charges. Dependence of the average displacement charge $\langle Q_d \rangle$ on the applied voltage is shown in Fig. 4 *C*. The constant term in the linear fit of this dependence corresponds to the state-dependent contribution of the protein to the displacement charge. Difference in the constant terms between the resting and activated states of NavAb according to Eq. 6 gives us an estimated gating charge Q_g^d of $8.21 \pm 0.17e$.

As a second approach to estimate gating charge for the whole channel, we used the method that employs CompEL simulations (31). This approach relies on simulating double-bilayer systems constructed from two copies of a single-bilayer system such that one of them is mirrored against the xy plane (Fig. 5 *A*). The number of ions in the compartments separated by the membranes is set to different values so that one compartment has an excess charge of q_{exc}. The CompEL algorithm retains this charge imbalance and thereby induces a sustainable transmembrane voltage, which can be inferred from the one-dimensional profiles of the electrostatic potential along the z axis of the system. We calculated the potential profiles at various values of q_{exc} by double integration of the overall charge distribution (31) as shown in Fig. 5 *B* and defined transmembrane voltage as the difference in the bulk potential between the compartments. As described by Eq. 7, the transmembrane voltage is induced by the intercompartment charge imbalance that consists of the ionic (q_{exc}) and the protein-associated (q_p) contributions. Since the latter depends on the activation state, different levels of q_{exc} have to be imposed to reach a comparable level of the transmembrane voltage in the systems with the channel in the resting and activated states (Fig. 5 *B*). Fig. 5 *C* shows dependence of the transmembrane voltage on q_{exc}. Fitting of these data by Eq. 7 allows for extraction of q_p values associated with the resting and activated states of NavAb. In turn, the difference in q_p between the states reports on the gating charge according to Eq. 8. The membrane capacitance C_m, as an independent fitting parameter in Eq. 7, was found largely independent of the protein activation state, with values of 8 ± 0.9 and $7.5 \pm 0.3\ e/V$ in the resting and activated states, respectively. Linear fits of the data by Eq. 7 gave values of $q_p^r = -14.48 \pm 0.13e$ and $q_p^a = -6.54 \pm 0.07e$ for the resting and activated states, respectively. Finally, the gating charge Q_g^d was found to be of $7.94 \pm 0.14e$.

Note that the two system-level methods give similar estimates of the gating charge of around $8e$. This value is close to the mean value of Q_g^w obtained via water-molecule

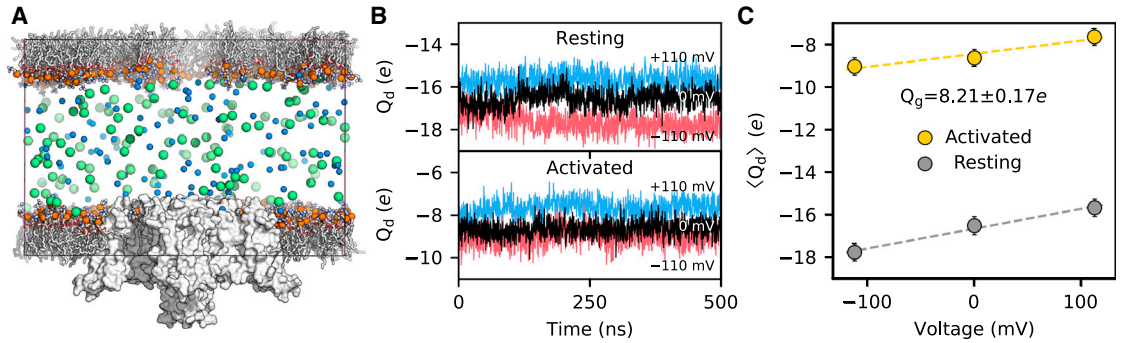

FIGURE 4 Gating charge of NavAb calculated through the displacement-charge method. (*A*) Positioning of the system in the simulation box for transferrable displacement-charge calculations. The protein is shown as white surface, and Cl^- and Na^+ as green and blue spheres, respectively. Edges of the box are highlighted. (*B*) Time course of the displacement charge in the systems with NavAb in the resting and activated states at 0 (*black*), −110 (*red*), and +110 mV (*blue*) transmembrane voltages. (*C*) Dependence of the average displacement charge on transmembrane voltage applied to NavAb in the activated (*gold*) and resting (*gray*) states. Gating charge (Q_g) was calculated as the difference between constant terms in linear fittings (indicated by *dashed lines*) of the data for the activated and resting states. Error bars indicate standard deviation. To see this figure in color, go online.

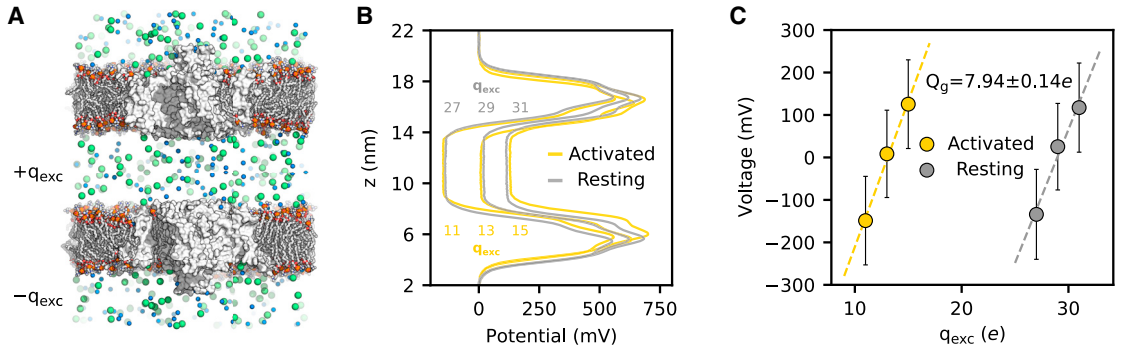

FIGURE 5 Gating charge of NavAb calculated through the CompEL method. (*A*) A snapshot of a CompEL system. The protein is shown as white surface, and Cl^- and Na^+ as green and blue spheres, respectively. Two copies of the protein are embedded into the membranes in an antiparallel orientation. The excess charge q_{exc} is induced by replacing an according number of Cl^- ions between the compartments separated by the membranes. The CompEL algorithm sustains the resulting charge imbalance during the simulation. (*B*) Distribution of the electrostatic potential along the z dimension of the system, as calculated by double integration of the overall charge distribution, is shown for the systems with NavAb in the resting (*gray*) and activated (*gold*) states. Values of q_{exc} are indicated. (*C*) Dependence of transmembrane voltage on q_{exc} is shown for systems with NavAb in the resting (*gray*) and activated (*gold*) states. The dependence was fitted by Eq. 7, and the difference in the resulting q_p values was used as an estimate of the gating charge (Q_g). The fit is shown as dashed line, and error bars indicate standard deviation. To see this figure in color, go online.

voltage fraction and is higher than the residue-based estimation Q_g^r (Table 2). The latter is likely underestimated due to lower contribution of R1 and R2 compared with the water-based scheme (Table 1). The gating charge of 8e is noticeably lower than experimental estimates of Q_g around 12e in eukaryotic (68) or 16e in bacterial (69) Nav channels, indicating incomplete representation of the VSD activation cycle by the existing activated and resting state structures of NavAb (43). Considering the difference in the electrostatic-potential distribution between these structures, we propose that a deeper resting state would be more favorable than a higher activated state (Fig. 2).

Electrostatics and voltage coupling in Nav1.5

In contrast to bacterial Nav channels, which are formed by four identical subunits, VSDs of eukaryotic Nav channels differ in their primary sequence, although they preserve the overall structural organization. To eventually test whether the variation in amino acid composition of VSDs could lead to a difference in their voltage coupling, we first quantified electrostatics in a mammalian cardiac channel Nav1.5. Fig. 6 *A* shows the distribution of the electrostatic potential along VSDs of the activated Nav1.5 that was simulated at different transmembrane voltages. In the intracellular vestibule of VSD1 and VSD2, the potential is negative, dropping below −200 mV just below the HCS, when no voltage is applied (Fig. 6 *A*). The potential well in this region is less pronounced in VSD3 and almost vanishes in VSD4 (Fig. 6 *A*). In the extracellular half, the potential distribution is rather shallow in all VSDs, with a moderate potential well at about 15 Å above the HCS. Concerning the central part of the VSDs, both VSD3 and VSD4 have a prominent surge in the potential at both intracellular and extracellular sides of the HCS (Fig. 6 *A*). The resulting peak in the potential, which rises higher than 300 mV, would create an energetic barrier for cation permeation through the gating pores formed by these VSDs, in contrast to VSD1 and VSD2 that lack such a barrier. Thus, our data indicate clear separation of VSDs of Nav1.5 into two classes defined by their electrostatic-potential distribution. On the one hand, the negative-potential well in the intracellular vestibule together with the absence of a prominent peak in the potential in the HCS suggest a cation-selective gating-pore current for VSD1 and VSD2 in the activated state. On the other hand, the shallow potential distribution in the vestibules and prominent electrostatic barrier for cations in the HCS suggests less pronounced cation conduction through VSD3 and VSD4 in the activated state. Furthermore, the presence of the electrostatic barrier in VSD3 and VSD4 might contribute, in addition to the immobilization by the inactivation particle, to their slower deactivation kinetics compared with the barrierless VSD1 and VSD2 (70). Interestingly, comparison of NavAb (Fig. 2 *B*) with Nav1.5 (Fig. 6 *A*) in the activated state demonstrates that the intracellular half of the NavAb VSD with its negative-potential well is more similar to VSD1 and VSD2, whereas its positive peak in the extracellular part is more like VSD3 and VSD4, thus indicating variation in the electrostatics between bacterial and eukaryotic VSDs.

Using the electrostatic-potential profiles, we then calculated the profiles of voltage fraction sensed by water within the VSDs of Nav1.5 (Fig. 6 *B*). Similar to the activated VSD of NavAb, the voltage fraction deviated from its bulk values in the central part of the Nav1.5 VSDs starting from around 8 Å below to about 15 Å above the HCS. However, the details of the voltage-fraction distribution differ across the VSDs. In particular, in the intracellular half, VSD1, VSD3, and VSD4 demonstrate a drop in the voltage fraction that rises again, in contrast to VSD2, whose voltage fraction goes down monotonically upon approaching the HCS

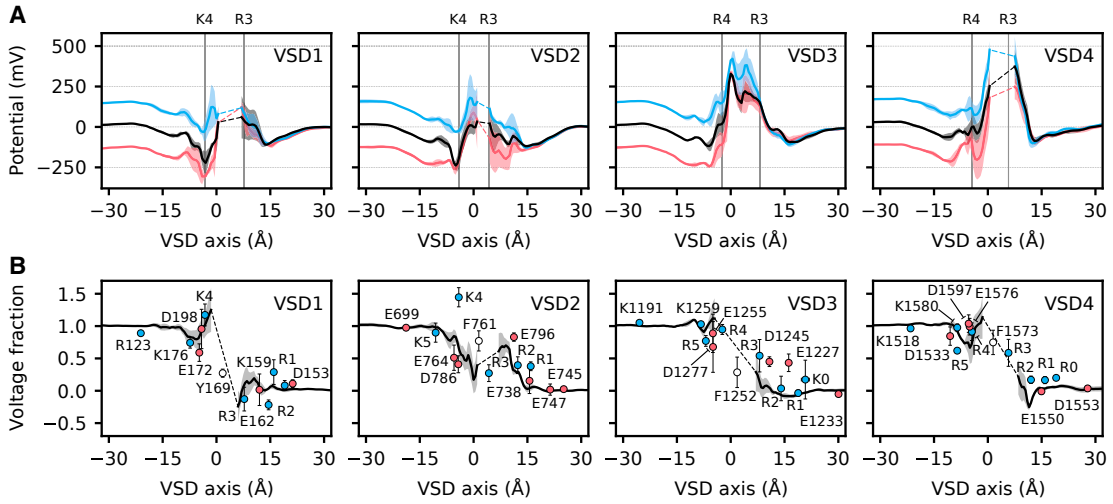

FIGURE 6 Distribution of electrostatic potential and voltage fraction within VSDs of Nav1.5. (*A*) Electrostatic potential in the hydrated regions of VSDs of Nav1.5 in the activated state at 0 (*black*), −140 (*red*), and +140 mV (*blue*) transmembrane voltages. Average positions of the gating arginines that flank the HCS are indicated by vertical lines. (*B*) Fraction of voltage sensed by water and selected residues within the VSDs. Profiles of the voltage fraction sensed by water molecules are shown in black. Data points report on the voltage fraction sensed by labeled charged residues of the VSDs. Data for positively and negatively charged residues are shown in blue and red, respectively. (*A* and *B*) Shaded areas and whiskers indicate the standard error of mean, as calculated for three independent replicas. Dashed lines are drawn for visual guidance through the low-hydrated (hydrated in < 2 replicas) region, which is characterized by high (> 150 mV for the potential and > 0.3 for voltage fraction) standard error of mean. The VSD axis is centered at the HCS. To see this figure in color, go online.

(Fig. 6 *B*). Together with a steady increase in voltage fraction in its extracellular part toward the HCS, this makes VSD2 the most similar to the VSD of NavAb. A monotonic increase in the voltage fraction is also observed in the extracellular part of VSD3, whereas the profiles of VSD1 and VSD4 demonstrate alternating directions upon reaching the HCS from the extracellular side. Finally, in VSD1, the whole transmembrane voltage drops across a region of about 5 Å width, indicating the strongest focusing of the electric field among all the Nav1.5 VSDs.

The voltage fraction measured directly for residues pointing toward the VSDs' interior of Nav1.5 is shown in Fig. 6 *B*. Except for three outliers (K4 in VSD2, and D1245 and E1227 in VSD3), the residue-sensed voltage fractions match well with the profile calculated for water molecules within the VSDs. In particular, a conserved pair of a glutamate and aspartate that form the INC senses full transmembrane voltage in VSD4 (E1576 and D1597), its major part in VSD1 (E172 and D198) and VSD3 (E1255 and D1277), and only half of it in VSD2 (E764 and D786). A resting-state structure of Nav1.5 is still missing, thus precluding comparison of the activated and resting states of the channel. However, the variability in the voltage fraction sensed by the INC in the activated state in the four VSDs may suggest different contributions of this pair of acidic residues to the overall gating charge of Nav1.5. Furthermore, assuming similar voltage-fraction distributions for the resting states of the VSD2 of Nav1.5 and the VSD of NavAb, we propose that the INC would contribute prominently to the gating charge of at least one domain in the eukaryotic channel as it does in the bacterial one (Table 1). Interestingly, the third gating arginine, R3, situated just above the HCS, experiences roughly half of the transmembrane voltage in VSD3 and VSD4, a slightly smaller fraction in VSD2, and virtually no voltage in VSD1. In excellent agreement with our results, an earlier experimental study on Nav1.4 reported a voltage fraction of 0.44 for S1427 that is located close to R3 of VSD4 in the activated state (12). Recently, VSD1 of Nav1.7 has been resolved in a deactivated state (46), where all the gating arginines were located below the HCS. Based on this structure as well as on our analysis of the resting-state structure of NavAb, we predict that a full downward transition of R3 in VSD1 of Nav1.5 would result in an about 1*e* contribution to the whole gating charge. In other VSDs, this contribution will be smaller, constituting around 0.5*e* in VSD3 and VSD4. Such qualitative speculations are, however, precluded in the case of the gating residues above R3, as the voltage fraction that they would experience in the resting state can be affected by state-dependent electric-field reshaping as in the case of NavAb.

DISCUSSION

Coupling of VSDs to the transmembrane voltage underlies the mechanism of activation and deactivation in voltage-gated ion channels. The complex shape of the electric field within VSDs and its important role in the activation process and associated gating charge has long been recognized (10). However, previous computational studies reported only a

minute difference of the voltage-coupling distribution across VSDs in different channels and activation states (15,16,18). Using low-resolution electrostatics calculations, these studies exhibited virtually featureless profiles of voltage coupling that monotonously decreased across the VSD (15–18). By contrast, high-resolution quantification of VSD electrostatics with *g_elpot* allowed us to detect prominent state-, isoform-, and domain-specific reshaping of the electric field within VSDs of Nav channels. In particular, we found that the region of the focused electric field can noticeably vary across different VSDs in the range of 5 Å as in VSD1 of Nav1.5 to more than 20 Å as in VSD2. Whereas the former length is close to early experimental predictions (10,13), the latter is closer to previous low-resolution calculations (15–18). Such unequal distribution underlies variation in the voltage coupling of gating residues. Due to wider focusing region, both R3 and R4 of NavAb in the activated state sense roughly half of the applied voltage (Fig. 3), implying that the VSD deactivation would be directly governed by both of these residues. Similarly, R3 is well primed to respond to the applied voltage in VSD2, VSD3, and VSD4, but less so in VSD1, of Nav1.5 (Fig. 6 *B*). Note the case of R3 in VSD4, where our calculated voltage fraction of about 0.5 sensed in the residue-localization site is in excellent agreement with an experimental value of 0.44 measured in Nav1.4 (12).

Strikingly, we observed a dramatic reshaping of the electric field in the VSD of NavAb upon transition between the structurally resolved activation states (Fig. 3). In particular, the excessive sensitivity of the INC in the resting state to the transmembrane voltage (Fig. 3 *A*), likely caused by the voltage-induced rearrangement of salt bridges (Fig. S2), resulted in a pronounced negative contribution of E59 and D80 to the gating charge in NavAb (Table 1). This leads to an about 1*e* reduction in the overall gating charge that is otherwise created by gating arginines, mainly by R2 and R3 (Table 1). Thus, state-dependent reshaping of the electric field notably affects the observed gating charge not only via gating residues but also by relatively static elements of the VSD.

Our calculations show that the gating charge associated with the transition of NavAb between the structurally resolved resting and activated states constitutes about 8*e* (Table 2). This value is significantly lower than experimental estimates of about 16*e* in a bacterial NaChBac (69) and of about 12*e* in skeletal muscle Nav channel (68). Thus, our results indicate that at least one of the resolved structures might represent an intermediate state of the VSD activation in NavAb. Similarly, a recent study (34) on a voltage-gated phosphatase Ci-VSP demonstrated that its VSD could adopt both a deeper resting ("down-minus") and higher activated ("up-plus") conformations relative to the resolved structures (33). Moreover, these results are in accord with another study on NavAb that proposed the existence of a higher activated and deeper resting state based on in-silico-generated models of the VSD to comply with the gating-charge measurements (63). Based on the analysis of the electrostatic-potential distribution (Fig. 2), we propose that a deeper resting state would be both kinetically and thermodynamically more plausible than a higher activated state. Notably, such a deeper resting state has been recently resolved for VSD1 of Nav1.7, where the outermost gating arginine R1 occupies the GCTC below the HCS (46), similar to the resting state of potassium channels (16,17,32,71–74). We would like to note that in the case where VSD activation starts from the deeper resting state, the detailed contribution of the residues into the gating charge could deviate from those obtained here (Table 1), owing to a possible electric-field reshaping upon transition between different resting states. Although cross-linking experiments (75) on another bacterial homolog NaChBac and in silico models (76) guided by these experiments propose extracellular localization of R1 in the resting state, gating-pore currents were detected in R1C mutants, indicating localization of R1 deeper in the HCS (77). Thus, we propose that similar to Kv channels (74), VSDs of Nav channels can adopt multiple resting states at different levels of membrane polarization.

Our analysis of electrostatics reveals further details of the mechanism of the gating-pore current, which is associated with a number of channelopathies (28), e.g., dilated cardiomyopathy caused by mutations in VSDs of the cardiac Nav1.5 (78,79). Although electrostatics plays a critical role in ion conduction and selectivity of ion channels (80–82), we note that our discussion on ion conduction through the gating pore omits effects of shorter-range interactions that may modify energetics of ion permeation. Our results, however, provide information that can be used in studies focused on the gating-pore conduction to decompose energetics of ion permeation into electrostatic and nonelectrostatic contributions. We observed state-dependent electrostatic-potential distributions along the VSD of NavAb (Fig. 2). Specifically, the smoothly distributed negative potential in the resting state contrasts with the one in the activated state that is characterized by a prominent positive barrier in the center of the VSD (Fig. 2). This barrier coincides with the one identified for Na^+ permeation in the R3G mutant of NavAb in the activated state (29). These results suggest that the energetics of ion permeation through the gating pore could depend on the activation state of the VSD. Furthermore, we observed a notable variation in the VSD electrostatics not only between different isoforms of Nav channels but also between homologous domains within a single channel. Based on the features in their electrostatic-potential distribution, VSDs of Nav1.5 can be split into two classes. In particular, VSD1 and VSD2 demonstrate notably negative potential in the intracellular vestibules and lack a clear barrier in their central parts. By contrast, VSD3 and VSD4 have a shallow potential distribution in the vestibules but

demonstrate prominent peaks at the HCS. Thus, we propose that in the activated state, VSD1 and VSD2 of Nav1.5 are more susceptible to gating-pore conduction than VSD3 and VSD4, in line with a higher number of naturally occurring R3 mutations associated with cardiac pathologies in the first two VSDs (78,79). Of note, VSD-mediated current can be induced by pulsed electric field in wild-type channels (24), with the pores partially formed by lipids, implying that their ion selectivity could additionally be affected by membrane lipid composition as in proteolipidic pores of ion-conducting lipid scramblases (83). However, naturally occurring gating-pore currents are mainly associated with charge-neutralizing mutations of the gating residues (28). Thus, R3 mutations (84,85) that lead to gating-pore currents through VSD1 and VSD2 in the activated state would further decrease the electrostatic potential in the HCS, leading to a more pronounced cation conduction. Although negative potential in the vestibules of all VSDs studied here clearly indicates their preference for cations, the demonstrated variation of the VSD electrostatics implies that ion selectivity of the gating-pore current could also vary across different VSDs. In line with this notion, a recent study on a mutant Ci-VSP reported a unique anion-selective gating-pore conduction (86), highlighting the impact of the detailed electrostatic distribution on the ion selectivity of gating-pore currents. Our findings, therefore, emphasize the fact that each VSD possesses a unique fingerprint of electrostatic distribution and voltage coupling that affects its ion selectivity and activation energetics.

CONCLUSIONS

In this study, we scrutinized electrostatics of VSDs in Nav channels to get insight into their voltage coupling and gating charge of activation. We found that each VSD is characterized by a unique distribution of the electric field that additionally depends on the activation state. This leads not only to variations in the strength of electric-field focusing across different domains and isoforms but also to prominently variable distributions of voltage coupling among VSDs. We also found that state-dependent reshaping of the electric field could result in prominent contributions of relatively static acidic residues to the overall gating charge. Moreover, our gating-charge calculations and electrostatics quantification suggest existence of a deeper resting state of NavAb upon hyperpolarization, with respect to the resolved structures. Finally, the notable variation of electrostatic-potential distribution observed here implies variation in ion-conduction properties of gating-pore currents mediated by VSDs in different states and isoforms. In conclusion, our results reveal effects of electric-field reshaping on the energetics of VSD activation and highlight the importance of a detailed quantification of electrostatics for a better understanding of ion-channel function in health and disease.

SUPPORTING MATERIAL

Supporting material can be found online at https://doi.org/10.1016/j.bpj.2023.04.013.

AUTHOR CONTRIBUTIONS

A.Y.K. conceived the study, designed and performed the research, and drafted the manuscript. A.Y.K. and J.-P.M. wrote the final version of the paper.

ACKNOWLEDGMENTS

The authors thank Drs. Yulia Kostritskaia, Claudia Alleva, and Christoph Fahlke for useful comments on the manuscript and Dr. Bassam Haddad for language editing. This work was supported by the Deutsche Forschungsgemeinschaft (German Research Foundation) to J.-P.M. (MA 7525/1-2, as part of the Research Unit FOR 2518, DynIon, project P4, and MA 7525/2-1, as part of the Research Unit FOR 6046, project P2), by the Jülich-Aachen Research Alliance Center for Simulation and Data Science (JARA-CSD) School for Simulation and Data Science (SSD), and by a grant from the Interdisciplinary Centre for Clinical Research within the faculty of Medicine at the RWTH Aachen University (IZKF TN1-3/IA532003). The authors gratefully acknowledge the computing time granted through JARA on the supercomputer JURECA at Forschungszentrum Jülich and the supercomputer CLAIX at RWTH Aachen University.

DECLARATION OF INTERESTS

The authors declare no competing interests.

REFERENCES

1. Freites, J. A., and D. J. Tobias. 2015. Voltage sensing in membranes: from macroscopic currents to molecular motions. *J. Membr. Biol.* 248:419–430. https://doi.org/10.1007/s00232-015-9805-x.
2. Catterall, W. A., G. Wisedchaisri, and N. Zheng. 2017. The chemical basis for electrical signaling. *Nat. Chem. Biol.* 13:455–463. https://doi.org/10.1038/nchembio.2353.
3. Groome, J. R., and L. Bayless-Edwards. 2020. Roles for countercharge in the voltage sensor domain of ion channels. *Front. Pharmacol.* 11:160. https://doi.org/10.3389/fphar.2020.00160.
4. Armstrong, C. M., and F. Bezanilla. 1973. Currents related to movement of the gating particles of the sodium channels. *Nature.* 242:459–461. https://doi.org/10.1038/242459a0.
5. Bezanilla, F. 2018. Gating currents. *J. Gen. Physiol.* 150:911–932. https://doi.org/10.1085/jgp.201812090.
6. Seoh, S. A., D. Sigg, F. Bezanilla…, 1996. Voltage-sensing residues in the S2 and S4 segments of the Shaker K^+ channel. *Neuron.* 16:1159–1167. https://doi.org/10.1016/s0896-6273(00)80142-7.
7. Ishida, I. G., G. E. Rangel-Yescas, …, L. D. Islas. 2015. Voltage-dependent gating and gating charge measurements in the Kv1.2 potassium channel. *J. Gen. Physiol.* 145:345–358. https://doi.org/10.1085/jgp.201411300.
8. Sigworth, F. J. 1994. Voltage gating of ion channels. *Q. Rev. Biophys.* 27:1–40. https://doi.org/10.1017/s0033583500002894.
9. Roux, B. 1997. Influence of the membrane potential on the free energy of an intrinsic protein. *Biophys. J.* 73:2980–2989.
10. Islas, L. D., and F. J. Sigworth. 2001. Electrostatics and the gating pore of Shaker potassium channels. *J. Gen. Physiol.* 117:69–89. https://doi.org/10.1085/jgp.117.1.69.

11. Asamoah, O. K., J. P. Wuskell, …, F. Bezanilla. 2003. A fluorometric approach to local electric field measurements in a voltage-gated ion channel. *Neuron.* 37:85–97. https://doi.org/10.1016/s0896-6273(02)01126-1.

12. Nguyen, T. P., and R. Horn. 2002. Movement and crevices around a sodium channel S3 segment. *J. Gen. Physiol.* 120:419–436. https://doi.org/10.1085/jgp.20028636.

13. Ahern, C. A., and R. Horn. 2005. Focused electric field across the voltage sensor of potassium channels. *Neuron.* 48:25–29. https://doi.org/10.1016/j.neuron.2005.08.020.

14. Jogini, V., and B. Roux. 2007. Dynamics of the Kv1.2 voltage-gated K^+ channel in a membrane environment. *Biophys. J.* 93:3070–3082. https://doi.org/10.1529/biophysj.107.112540.

15. Khalili-Araghi, F., V. Jogini, …, K. Schulten. 2010. Calculation of the gating charge for the Kv1.2 voltage-activated potassium channel. *Biophys. J.* 98:2189–2198. https://doi.org/10.1016/j.bpj.2010.02.056.

16. Delemotte, L., M. Tarek, …, W. Treptow. 2011. Intermediate states of the Kv1.2 voltage sensor from atomistic molecular dynamics simulations. *Proc. Natl. Acad. Sci. USA.* 108:6109–6114. https://doi.org/10.1073/pnas.1102724108.

17. Delemotte, L., M. A. Kasimova, …, V. Carnevale. 2015. Free-energy landscape of ion-channel voltage-sensor-domain activation. *Proc. Natl. Acad. Sci. USA.* 112:124–129. https://doi.org/10.1073/pnas.1416959112.

18. Souza, C. S., C. Amaral, and W. Treptow. 2014. Electric fingerprint of voltage sensor domains. *Proc. Natl. Acad. Sci. USA.* 111:17510–17515. https://doi.org/10.1073/pnas.1413971111.

19. Starace, D. M., and F. Bezanilla. 2004. A proton pore in a potassium channel voltage sensor reveals a focused electric field. *Nature.* 427:548–553.

20. Kostritskii, A. Y., C. Alleva, …, J.-P. Machtens. 2021. g_elpot: a tool for quantifying biomolecular electrostatics from molecular dynamics trajectories. *J. Chem. Theory Comput.* 17:3157–3167. https://doi.org/10.1021/acs.jctc.0c01246.

21. Etges, A., N. Hellmig, …, U. I. Scholl. 2022. A novel homozygous KLHL3 mutation as a cause of autosomal recessive pseudohypoaldosteronism type II diagnosed late in life. *Nephron.* 146:418–428. https://doi.org/10.1159/000521626.

22. Patra, P., and Y. Q. Gao. 2022. Sequence-specific structural features and solvation properties of transcription factor binding DNA motifs: insights from molecular dynamics simulation. *J. Phys. Chem. B.* 126:9187–9206. https://doi.org/10.1021/acs.jpcb.2c05749.

23. Zhuang, Y., C. M. Noviello, …, E. Lindahl. 2022. Differential interactions of resting, activated, and desensitized states of the α7 nicotinic acetylcholine receptor with lipidic modulators. *Proc. Natl. Acad. Sci. USA.* 119. e2208081119. https://doi.org/10.1073/pnas.2208081119.

24. Rems, L., M. A. Kasimova, …, L. Delemotte. 2020. Pulsed electric fields can create pores in the voltage sensors of voltage-gated ion channels. *Biophys. J.* 119:190–205. https://doi.org/10.1016/j.bpj.2020.05.030.

25. Jurkat-Rott, K., J. Groome, and F. Lehmann-Horn. 2012. Pathophysiological role of omega pore current in channelopathies. *Front. Pharmacol.* 3:112. https://doi.org/10.3389/fphar.2012.00112.

26. Tarek, M., and L. Delemotte. 2013. Omega currents in voltage-gated ion channels: what can we learn from uncovering the voltage-sensing mechanism using MD simulations? *Acc. Chem. Res.* 46:2755–2762. https://doi.org/10.1021/ar300290u.

27. Moreau, A., P. Gosselin-Badaroudine, and M. Chahine. 2014. Biophysics, pathophysiology, and pharmacology of ion channel gating pores. *Front. Pharmacol.* 5:53. https://doi.org/10.3389/fphar.2014.00053.

28. Moreau, A., P. Gosselin-Badaroudine, and M. Chahine. 2014. Molecular biology and biophysical properties of ion channel gating pores. *Q. Rev. Biophys.* 47:364–388. https://doi.org/10.1017/S0033583514000109.

29. Jiang, D., T. M. Gamal El-Din, …, W. A. Catterall. 2018. Structural basis for gating pore current in periodic paralysis. *Nature.* 557:590–594. https://doi.org/10.1038/s41586-018-0120-4.

30. Roux, B. 2008. The membrane potential and its representation by a constant electric field in computer simulations. *Biophys. J.* 95:4205–4216. https://doi.org/10.1529/biophysj.108.136499.

31. Machtens, J.-P., R. Briones, …, C. Fahlke. 2017. Gating charge calculations by computational electrophysiology simulations. *Biophys. J.* 112:1396–1405. https://doi.org/10.1016/j.bpj.2017.02.016.

32. Jensen, M. Ø., V. Jogini, …, D. E. Shaw. 2012. Mechanism of voltage gating in potassium channels. *Science.* 336:229–233. https://doi.org/10.1126/science.1216533.

33. Li, Q., S. Wanderling, …, E. Perozo. 2014. Structural mechanism of voltage-dependent gating in an isolated voltage-sensing domain. *Nat. Struct. Mol. Biol.* 21:244–252. https://doi.org/10.1038/nsmb.2768.

34. Shen, R., Y. Meng, …, E. Perozo. 2022. Mechanism of voltage gating in the voltage-sensing phosphatase Ci-VSP. *Proc. Natl. Acad. Sci. USA.* 119. e2206649119. https://doi.org/10.1073/pnas.2206649119.

35. Kutzner, C., H. Grubmüller, …, U. Zachariae. 2011. Computational electrophysiology: the molecular dynamics of ion channel permeation and selectivity in atomistic detail. *Biophys. J.* 101:809–817. https://doi.org/10.1016/j.bpj.2011.06.010.

36. Kutzner, C., D. A. Köpfer, …, U. Zachariae. 2016. Insights into the function of ion channels by computational electrophysiology simulations. *Biochim. Biophys. Acta.* 1858:1741–1752. https://doi.org/10.1016/j.bbamem.2016.02.006.

37. Vickery, O. N., J.-P. Machtens, …, U. Zachariae. 2016. Structural mechanisms of voltage sensing in G protein-coupled receptors. *Structure.* 24:997–1007. https://doi.org/10.1016/j.str.2016.04.007.

38. Vickery, O. N., C. A. Carvalheda, U. Zachariae…, 2018. Intracellular transfer of Na^+ in an active-state G-protein-coupled receptor. *Structure.* 26:171–180.e2. https://doi.org/10.1016/j.str.2017.11.013.

39. Shen, H., Q. Zhou, …, N. Yan. 2017. Structure of a eukaryotic voltage-gated sodium channel at near-atomic resolution. *Science.* 355:eaal4326. https://doi.org/10.1126/science.aal4326.

40. Yan, Z., Q. Zhou, …, N. Yan. 2017. Structure of the Nav1.4-β1 complex from electric eel. *Cell.* 170:470–482.e11. https://doi.org/10.1016/j.cell.2017.06.039.

41. Pan, X., Z. Li, …, N. Yan. 2018. Structure of the human voltage-gated sodium channel Nav1.4 in complex with β1. *Science.* 362:eaau2486. https://doi.org/10.1126/science.aau2486.

42. Shen, H., D. Liu, …, N. Yan. 2019. Structures of human Nav1.7 channel in complex with auxiliary subunits and animal toxins. *Science.* 363:1303–1308. https://doi.org/10.1126/science.aaw2493.

43. Wisedchaisri, G., L. Tonggu, …, W. A. Catterall. 2019. Resting-state structure and gating mechanism of a voltage-gated sodium channel. *Cell.* 178:993–1003.e12. https://doi.org/10.1016/j.cell.2019.06.031.

44. Jiang, D., H. Shi, …, W. A. Catterall. 2020. Structure of the cardiac sodium channel. *Cell.* 180:122–134.e10. https://doi.org/10.1016/j.cell.2019.11.041.

45. Jiang, D., R. Banh, …, W. A. Catterall. 2021. Open-state structure and pore gating mechanism of the cardiac sodium channel. *Cell.* 184:5151–5162.e11. https://doi.org/10.1016/j.cell.2021.08.021.

46. Huang, G., Q. Wu, …, N. Yan. 2022. Unwinding and spiral sliding of S4 and domain rotation of VSD during the electromechanical coupling in Nav1.7. *Proc. Natl. Acad. Sci. USA.* 119. e2209164119. https://doi.org/10.1073/pnas.2209164119.

47. Huang, X., X. Jin, …, N. Yan. 2022. Structural basis for high-voltage activation and subtype-specific inhibition of human Nav1.8. *Proc. Natl. Acad. Sci. USA.* 119. e2208211119. https://doi.org/10.1073/pnas.2208211119.

48. Šali, A., and T. L. Blundell. 1993. Comparative protein modelling by satisfaction of spatial restraints. *J. Mol. Biol.* 234:779–815.

49. Abraham, M. J., T. Murtola, …, E. Lindahl. 2015. GROMACS: high performance molecular simulations through multi-level parallelism from laptops to supercomputers. *SoftwareX.* 1-2:19–25. https://doi.org/10.1016/j.softx.2015.06.001.

50. Parrinello, M., and A. Rahman. 1981. Polymorphic transitions in single crystals: a new molecular dynamics method. *J. Appl. Phys.* 52:7182–7190. https://doi.org/10.1063/1.328693.

51. Berendsen, H. J. C., J. P. M. Postma, …, J. R. Haak. 1984. Molecular dynamics with coupling to an external bath. *J. Chem. Phys.* 81:3684–3690. https://doi.org/10.1063/1.448118.

52. Bussi, G., D. Donadio, and M. Parrinello. 2007. Canonical sampling through velocity rescaling. *J. Chem. Phys.* 126:014101. https://doi.org/10.1063/1.2408420.

53. Essmann, U., L. Perera, …, L. G. Pedersen. 1995. A smooth particle mesh Ewald method. *J. Chem. Phys.* 103:8577–8593. https://doi.org/10.1063/1.470117.

54. Darden, T., D. York, and L. Pedersen. 1993. Particle mesh Ewald: an N ·log(N) method for Ewald sums in large systems. *J. Chem. Phys.* 98:10089–10092. https://doi.org/10.1063/1.464397.

55. Huang, J., S. Rauscher, …, A. D. MacKerell. 2017. CHARMM36m: an improved force field for folded and intrinsically disordered proteins. *Nat. Methods.* 14:71–73. https://doi.org/10.1038/nmeth.4067.

56. Klauda, J. B., R. M. Venable, …, R. W. Pastor. 2010. Update of the CHARMM all-atom additive force field for lipids: validation on six lipid types. *J. Phys. Chem. B.* 114:7830–7843. https://doi.org/10.1021/jp101759q.

57. Hess, B., H. Bekker, …, J. G. E. M. Fraaije. 1997. LINCS: a linear constraint solver for molecular simulations. *J. Comput. Chem.* 18:1463–1472.

58. Yoo, J., and A. Aksimentiev. 2012. Improved parametrization of Li^+, Na^+, K^+, and Mg^{2+} ions for all-atom molecular dynamics simulations of nucleic acid systems. *J. Phys. Chem. Lett.* 3:45–50. https://doi.org/10.1021/jz201501a.

59. Wolf, M. G., M. Hoefling, G. Groenhof…, 2010. g_membed: Efficient insertion of a membrane protein into an equilibrated lipid bilayer with minimal perturbation. *J. Comput. Chem.* 31:2169–2174. https://doi.org/10.1002/jcc.21507.

60. Michaud-Agrawal, N., E. J. Denning, …, O. Beckstein. 2011. A toolkit for the analysis of molecular dynamics simulations. *J. Comput. Chem.* 32:2319–2327. https://doi.org/10.1002/jcc.21787.

61. Gumbart, J., F. Khalili-Araghi, …, B. Roux. 2012. Constant electric field simulations of the membrane potential illustrated with simple systems. *Biochim. Biophys. Acta.* 1818:294–302. https://doi.org/10.1016/j.bbamem.2011.09.030.

62. Tao, X., A. Lee, …, R. MacKinnon. 2010. A gating charge transfer center in voltage sensors. *Science.* 328:67–73. https://doi.org/10.1126/science.1185954.

63. Amaral, C., V. Carnevale, …, W. Treptow. 2012. Exploring conformational states of the bacterial voltage-gated sodium channel NavAb via molecular dynamics simulations. *Proc. Natl. Acad. Sci. USA.* 109:21336–21341. https://doi.org/10.1073/pnas.1218087109.

64. Payandeh, J., T. M. Gamal El-Din, …, W. A. Catterall. 2012. Crystal structure of a voltage-gated sodium channel in two potentially inactivated states. *Nature.* 486:135–139. https://doi.org/10.1038/nature11077.

65. Gamal El-Din, T. M., G. Q. Martinez, …, W. A. Catterall. 2013. A gating charge interaction required for late slow inactivation of the bacterial sodium channel NavAb. *J. Gen. Physiol.* 142:181–190. https://doi.org/10.1085/jgp.201311012.

66. Kasimova, M. A., E. Lindahl, and L. Delemotte. 2018. Determining the molecular basis of voltage sensitivity in membrane proteins. *J. Gen. Physiol.* 150:1444–1458. https://doi.org/10.1085/jgp.201812086.

67. Pathak, M. M., V. Yarov-Yarovoy, E. Y. Isacoff…, 2007. Closing in on the resting state of the Shaker K^+ channel. *Neuron.* 56:124–140. https://doi.org/10.1016/j.neuron.2007.09.023.

68. Hirschberg, B., A. Rovner, J. Patlak…, 1995. Transfer of twelve charges is needed to open skeletal muscle Na^+ channels. *J. Gen. Physiol.* 106:1053–1068. https://doi.org/10.1085/jgp.106.6.1053.

69. Kuzmenkin, A., F. Bezanilla, and A. M. Correa. 2004. Gating of the bacterial sodium channel, NaChBac: voltage-dependent charge movement and gating currents. *J. Gen. Physiol.* 124:349–356. https://doi.org/10.1085/jgp.200409139.

70. Varga, Z., W. Zhu, J. R. Silva…, 2015. Direct measurement of cardiac Na^+ channel conformations reveals molecular pathologies of inherited mutations. *Circ. Arrhythm. Electrophysiol.* 8:1228–1239. https://doi.org/10.1161/CIRCEP.115.003155.

71. Lin, M.-c. A., J.-Y. Hsieh, D. M. Papazian…, 2011. R1 in the Shaker S4 occupies the gating charge transfer center in the resting state. *J. Gen. Physiol.* 138:155–163. https://doi.org/10.1085/jgp.201110642.

72. Vargas, E., F. Bezanilla, and B. Roux. 2011. In search of a consensus model of the resting state of a voltage-sensing domain. *Neuron.* 72:713–720. https://doi.org/10.1016/j.neuron.2011.09.024.

73. Vargas, E., V. Yarov-Yarovoy, …, B. Roux. 2012. An emerging consensus on voltage-dependent gating from computational modeling and molecular dynamics simulations. *J. Gen. Physiol.* 140:587–594. https://doi.org/10.1085/jgp.201210873.

74. Catacuzzeno, L., L. Sforna, and F. Franciolini. 2020. Voltage-dependent gating in K channels: experimental results and quantitative models. *Pflugers Arch.* 472:27–47. https://doi.org/10.1007/s00424-019-02336-6.

75. DeCaen, P. G., V. Yarov-Yarovoy, W. A. Catterall…, 2011. Gating charge interactions with the S1 segment during activation of a Na^+ channel voltage sensor. *Proc. Natl. Acad. Sci. USA.* 108:18825–18830. https://doi.org/10.1073/pnas.1116449108.

76. Yarov-Yarovoy, V., P. G. DeCaen, …, W. A. Catterall. 2012. Structural basis for gating charge movement in the voltage sensor of a sodium channel. *Proc. Natl. Acad. Sci. USA.* 109:E93–E102. https://doi.org/10.1073/pnas.1118434109.

77. Gamal El-Din, T. M., T. Scheuer, and W. A. Catterall. 2014. Tracking S4 movement by gating pore currents in the bacterial sodium channel NaChBac. *J. Gen. Physiol.* 144:147–157. https://doi.org/10.1085/jgp.201411210.

78. Gosselin-Badaroudine, P., A. Moreau, and M. Chahine. 2014. Nav 1.5 mutations linked to dilated cardiomyopathy phenotypes: is the gating pore current the missing link? *Channels.* 8:90–94. https://doi.org/10.4161/chan.27179.

79. Moreau, A., and M. Chahine. 2018. A new cardiac channelopathy: from clinical phenotypes to molecular mechanisms associated with Nav1.5 gating pores. *Front. Cardiovasc. Med.* 5:139. https://doi.org/10.3389/fcvm.2018.00139.

80. Maffeo, C., S. Bhattacharya, …, A. Aksimentiev. 2012. Modeling and simulation of ion channels. *Chem. Rev.* 112:6250–6284. https://doi.org/10.1021/cr3002609.

81. Machtens, J.-P., D. Kortzak, …, C. Fahlke. 2015. Mechanisms of anion conduction by coupled glutamate transporters. *Cell.* 160:542–553. https://doi.org/10.1016/j.cell.2014.12.035.

82. Alleva, C., J.-P. Machtens, …, C. Fahlke. 2022. Molecular basis of coupled transport and anion conduction in excitatory amino acid transporters. *Neurochem. Res.* 47:9–22. https://doi.org/10.1007/s11064-021-03252-x.

83. Kostritskii, A. Y., and J.-P. Machtens. 2021. Molecular mechanisms of ion conduction and ion selectivity in TMEM16 lipid scramblases. *Nat. Commun.* 12:2826. https://doi.org/10.1038/s41467-021-22724-w.

84. Moreau, A., P. Gosselin-Badaroudine, …, M. Chahine. 2015. Gating pore currents are defects in common with two Nav1.5 mutations in patients with mixed arrhythmias and dilated cardiomyopathy. *J. Gen. Physiol.* 145:93–106. https://doi.org/10.1085/jgp.201411304.

85. Moreau, A., P. Gosselin-Badaroudine, …, M. Chahine. 2015. Mutations in the voltage sensors of domains I and II of Nav1.5 that are associated with arrhythmias and dilated cardiomyopathy generate gating pore currents. *Front. Pharmacol.* 6:301. https://doi.org/10.3389/fphar.2015.00301.

86. Shen, R., B. Roux, and E. Perozo. 2022. State dependent anionic pore currents conducted by single countercharge mutants in a voltage-sensing phosphatase. Preprint at bioRxiv. https://doi.org/10.1101/2022.04.04.487073.